Multibridge VO$_2$-Based Resistive Switching Devices in a Two-Terminal Configuration

Xing Gao, Thijs J. Roskamp, Timm Swoboda, Carlos M. M. Rosário, Sander Smink, Miguel Muñoz Rojo, and Hans Hilgenkamp*

Vanadium dioxide exhibits a hysteretic insulator-to-metal transition (IMT) near room temperature, forming the foundation for various forms of resistive switching devices. Usually, these are realized in the form of two-terminal bridge-like structures. The authors show here that by incorporating multiple, parallel VO$_2$ bridges in a single two-terminal device, a wider range of possible characteristics can be obtained, including a manifold of addressable resistance states. Different device configurations are studied, in which the number of bridges, the bridge dimensions, and the interbridge distances are varied. The switching characteristics of the multibridge devices are influenced by the thermal cross-talk between the bridges. Scanning thermal microscopy (SThM) is used to image the current distributions at various voltage/current bias conditions. This work presents a route to realize devices exhibiting highly nonlinear, multistate current–voltage characteristics, with potential applications in, e.g., tunable electronic components and novel, neuromorphic information processing circuitry.

1. Introduction

To overcome limitations of computing systems based on von Neumann architectures, like excessive data transfer between memory and logic units, neuromorphic device concepts that mimic the function of neurons and synapses are of particular interest.[1,2] The neuromorphic computing circuitry requires novel circuit elements with tunable resistance states, nonlinear response functions and, for the case of spiking neuromorphic circuitry, adaptable dynamic behavior.[1,3,4] VO$_2$ is an attractive candidate material to fulfill several of these roles, because it exhibits a near-room-temperature, hysteretic insulator-to-metal transition (IMT) with resistivity changes of several orders of magnitude.[5–10] The IMT can be tuned by chemical doping,[11] epitaxial strain,[12,13] and external stimuli.[14–16] Particularly, it can be triggered by electrical voltage/current and the associated Joule heating.[16–21] The electrical and thermal conductivity of VO$_2$ are highly temperature-dependent, leading to nonlinear dynamics in an electrothermal feedback loop.[22,23] Using such nonlinear behavior, Yi et al. have demonstrated a range of neuronic spiking patterns in VO$_2$-based neuromorphic circuits.[24] Furthermore, tunable multilevel resistive states have been achieved in single VO$_2$ bridges, with the outlook that devices with multiple parallel bridges may provide a higher degree of control.[20]

Here, we extend our studies on two-terminal VO$_2$ devices incorporating such multiple parallel bridges. To characterize the switching behavior, we perform both voltage-controlled and current-controlled measurements, which result in different current–voltage (I—V) characteristics as will be elucidated below. We have employed scanning thermal microscopy (SThM) to directly image the current distribution in the devices.[25] SThM uses a special thermo-resistive probe with high thermal sensitivity that enables the characterization of thermal phenomena on the sample surface with nanoscale spatial resolution.[26–28] For our VO$_2$ bridges, the local heating generated is directly linked to the current flow, due to Joule heating.[17,29]

2. Results and Discussion

2.1. VO$_2$-Based Double-Bridge Devices

In **Figure 1**a, the device configuration is sketched. The most basic version, previously reported,[20] consists of a single VO$_2$ bridge

X. Gao, T. J. Roskamp, C. M. M. Rosário, S. Smink, H. Hilgenkamp
Faculty of Science and Technology and MESA+ Institute for Nanotechnology
University of Twente
Enschede 7500 AE, The Netherlands
E-mail: h.hilgenkamp@utwente.nl

T. Swoboda, M. Muñoz Rojo
Department of Thermal and Fluid Engineering
Faculty of Engineering Technology
University of Twente
Enschede 7500 AE, The Netherlands

M. Muñoz Rojo
2D Foundry
Instituto de Ciencia de Materiales de Madrid (ICMM), CSIC
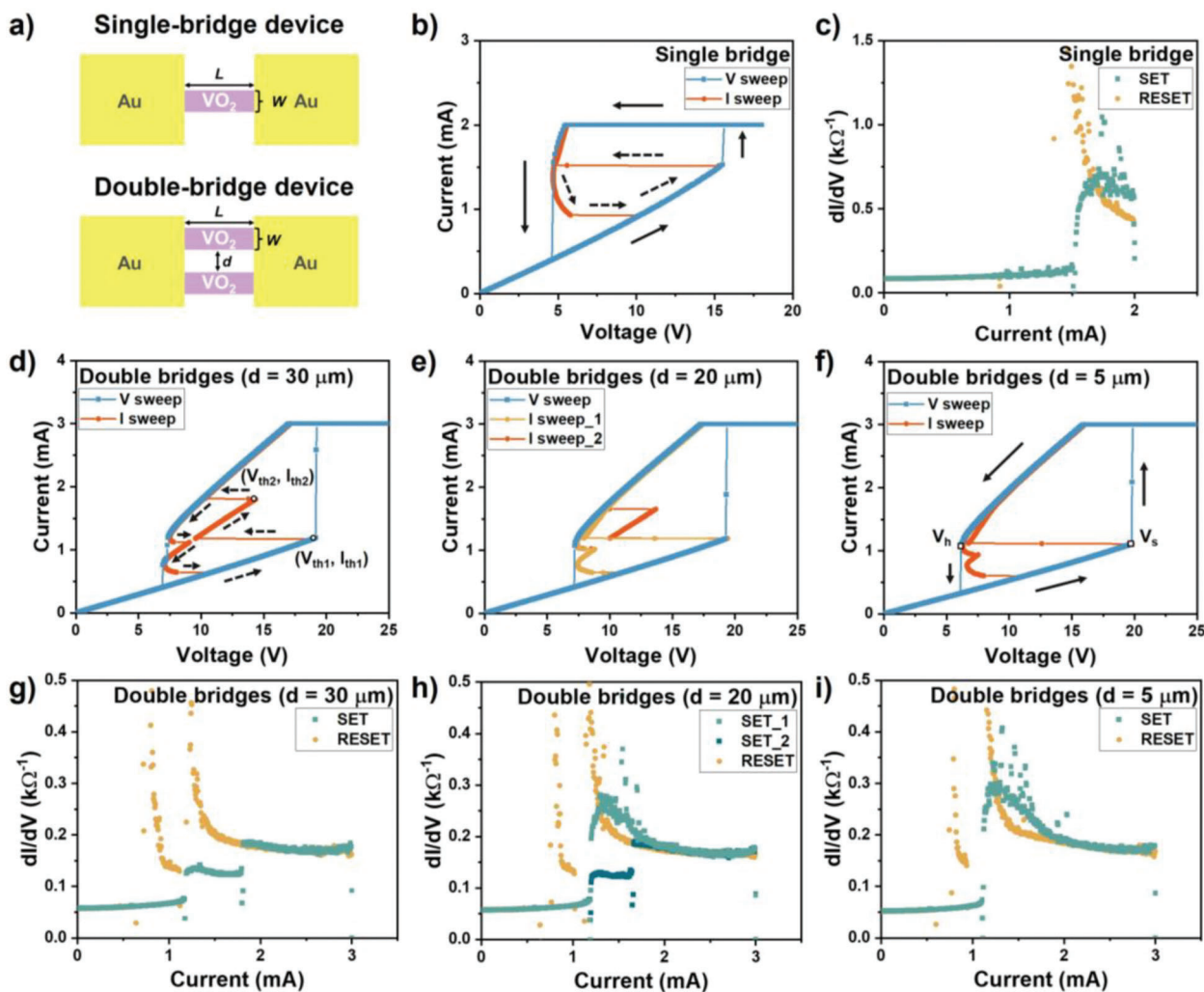Sor Juana Inés de la Cruz, 3, Madrid 28049, Spain

Figure 1. a) Schematic top-view of the VO_2-based single-bridge and double-bridge device. The width (W), length (L), and spacing (d) of the patterned VO_2 parallel bridges are as labeled. b) Voltage-controlled (direction indicated with solid arrows) and current-controlled (direction indicated with dashed arrows) I–V characteristics and c) differential conductance (dI/dV) as a function of applied current during the set and reset process of a single-bridge device ($L = 20$ μm, $W = 5$ μm). $I_{CC} = 2$ mA. Voltage-controlled and current-controlled I–V characteristics and of double-bridge devices ($L = 20$ μm, $W = 5$ μm) with different spacings: d) $d = 30$ μm, e) $d = 20$ μm, and f) $d = 5$ μm. $I_{CC} = 3$ mA. The terminology of threshold voltages (V_{th}) and currents (I_{th}) for current sweeps are indicated in (d). The terminology of set voltage (V_s) and hold voltage (V_h) for voltage sweeps are indicated in f). Differential conductance dI/dV during the set and reset process for corresponding devices: g) $d = 30$ μm, h) $d = 20$ μm, i) $d = 5$ μm. The range is selected to clearly see the conductance steps. See Figure S3 (Supporting Information) for the full vertical axis range of dI/dV values.

contacted in a two-terminal configuration. In the same figure, a double-bridge device is shown, in which the two-terminal configuration is maintained. However, this structure consists of two parallel bridges with length L, width W and interbridge spacing d. Later on, configurations with more than two bridges will be discussed as well. Figure 1b shows the switching characteristics of a single bridge, in voltage- and current-sweep mode, respectively. These data are in line with our previous report,[20] whereby it is noted that all measurements discussed here are conducted after a first forming cycle (Figure S1, Supporting Information). The electroforming process in the double-bridge devices follows the same underlying principles as the single-bridge devices. Moreover, with sufficient power, the forming effect takes place on both bridges, causing a decrease in the initial resistance of the bridges and the required power for switching (Figure S2, Supporting

Information). For a voltage-controlled sweep, the heating generated at the switching point (here at $V = 15$ V) increases abruptly by the sharp rise of the current, up to the compliance current (I_{CC}), which results in a sharp increase in dissipated power. For a current-controlled sweep, on the other hand, the heating develops more gradually due to the associated voltage drop and can be stabilized. On the reset path, using the current bias, a region with a negative differential resistance (NDR) can be identified. Figure 1c shows the numerically computed differential conductance dI/dV, for a limited range of values. Figure S3 (Supporting Information) shows the full scale of the differential conductance, including the NDR values.

Figure 1d–f shows measurements on a double-bridge structure with a fixed length ($L = 20$ μm) and width ($W = 5$ μm) for different values of the spacing between the bridges, i.e.,

**ADVANCED
SCIENCE NEWS**

www.advancedsciencenews.com

**ADVANCED
ELECTRONIC
MATERIALS**

www.advelectronicmat.de

30, 20, and 5 μm. Here, the difference between the current- and voltage-bias sweeps becomes extra apparent. While with a voltage bias, we again see a single, big increase in the current at the switching point, for the current bias we see—depending on the separation—multiple switches, as can be expected from a sequential switching of the individual bridges.

In the double-bridge devices, the switching behaviors of the parallel bridge devices are determined by the intrinsic IMT of individual bridges and the thermal interaction between them. In this work, several available knobs at a device level are tuned for manipulation of the switching behaviors. Double-bridge devices, multiple-bridge devices, and multiwidth-bridge devices are discussed in the following sections. Despite the rising complexity, there are some basic trends that have been observed. One is that more potential switches and intermediate resistive states can be achieved by adding more bridges in parallel.

Also, the spacing between bridges influences the number of switching events and the power required for subsequent switches. This is clear from Figure 1d–f and Figure S4 (Supporting Information). If the bridges are far away from each other, for example $d = 30$ μm (Figure 1d), the thermal cross-talk is small and the bridges switch individually and sequentially. In this case, a stable intermediate resistive state occurs. If the bridges are close to each other, for example $d = 5$ μm (Figure 1f), the heat dissipation of one bridge will affect the other greatly and both bridges will be triggered simultaneously, so that there is only one switching event during the set process. As shown in Figure 1e, there is a critical spacing value, in this experiment $d = 20$ μm, where the device shows simultaneous switching or individual switching randomly (see Figure S5 (Supporting Information) for the current-controlled $I–V$ curves for 20 cycles).

From the current-controlled $I–V$ characteristics, the differential conductance (dI/dV) of the measured devices is calculated and plotted as a function of applied current, see Figure 1g–i and Figure S3 (Supporting Information). The dI/dV values near the switching point or in the NDR region diverge to large positive and negative values. When the device resistance settles, the dI/dV should scale with the number of conductance paths available for the current.[30] Indeed, we see that when there is only one switch the change of differential conductance per switch is double to the case when there are two consecutive switching events.

Interestingly, there are several NDR regions in the current-controlled sweep, where the differential resistance (dV/dI) of the device is negative. NDR can generally be found in materials that form higher current density channels relative to the rest of the material under electrical stimuli.[31] The dynamical instabilities associated with NDR are of great interest for potential applications, such as selectors, threshold switches, amplifiers, and oscillators.[22] There are two types of NDR: a "snapback NDR" refers to a discontinuous transition from positive to negative differential resistance, while an "S-type NDR" refers to a smooth transition.[22,32] Li et al. reported a model of current-controlled NDR by explicitly accounting for a nonuniform current distribution in the oxide film and its impact on the effective circuit of the device.[33] In their model, the switching element is considered as a core–shell structure with a high current–density core represented by an archetype memristor and a low current–density shell represented by a resistor. The NDR characteristics are determined by the relative magnitudes of the shell resistance (R_S) and

the maximum negative differential resistance of the core (R_{NDR}), with S-type characteristics predicted for $R_S > R_{NDR}$ and snapback characteristics predicted for $R_S < R_{NDR}$. When both the core and the shell regions are modeled as archetype memristors with a temperature-dependent conductivity, the resulting NDR characteristics become combinations of S-type and snapback. These two types of responses are generic for materials with a significant temperature-dependent conductivity. Moreover, the behavior can be controlled by adjusting the material conductivity, device area, or ambient temperature.[32]

Both types of NRD response, and sometimes even more complex combinations of them, are observed in our devices. With the thermally induced IMT in VO$_2$, the dynamics and instabilities result from an electrothermal feedback loop, as the electrical and thermal properties are highly temperature-dependent.[4] In our devices, the snapback NDR is usually observed during the set process due to the sharp transition from low conductivity to high conductivity and the current redistribution between the bridges, while the S-type NDR is observed during the reset where the VO$_2$ bridges are experiencing a more gradual transition.[18,34] Moreover, the thermal cross-talk among the bridges will also lead to complex NDR characteristics.

Assuming that the voltage is equal across both bridges and decreases linearly along the device, the current can be determined from the Joule heating. Therefore, the current distribution and switching behavior in our multibridge devices can be visualized by mapping the Joule heating locally using SThM, as is shown in **Figure 2**a,b which shows that the bridges are switched individually under the applied current bias for the well-separated double-bridge device under study here. During the SThM scans, the device is set to stable intermediate resistive states by biasing at constant current values as shown in Figure 2c. The qualitative thermal maps obtained during the set process and the reset process maintaining constant measurement conditions are plotted in Figure 2d,e, respectively. In this, the SThM signal correlates with the temperature increase of the bridges. By increasing the bias current from zero to a value below the threshold current for switching I_{th}, the current distributes evenly over the two bridges (scan A). When one of the bridges switches, the heating is redistributed indicating that almost all the current flows through the bridge that has switched ON (scan B). By further increasing the bias current, there will be an increase in the current flowing through both bridges according to their differences in resistance and, potentially supported by heat transferred from the bridge with the highest current, also the remaining bridge switches to a low-resistance state (scan C).

The reset process is basically the inverse process of the set behavior, but follows a different trace, due to the hysteretic resistance versus temperature characteristics of the VO$_2$. Starting with two bridges in the low-resistance state (scan D), the right bridge is switched OFF when the current decreases (scan E), and finally the remaining bridge is also switched to the high-resistance state and the current is almost evenly distributed over both bridges again (scan F). While in principle the switching sequence between the two bridges for the set and reset process could be different, we see in Figure 2 as well as in all our other measurements thus far, that the order of switching back to the high-resistance state is the reverse of the switching events to the low-resistance state. The reset order is determined by the power for a bridge to be switched
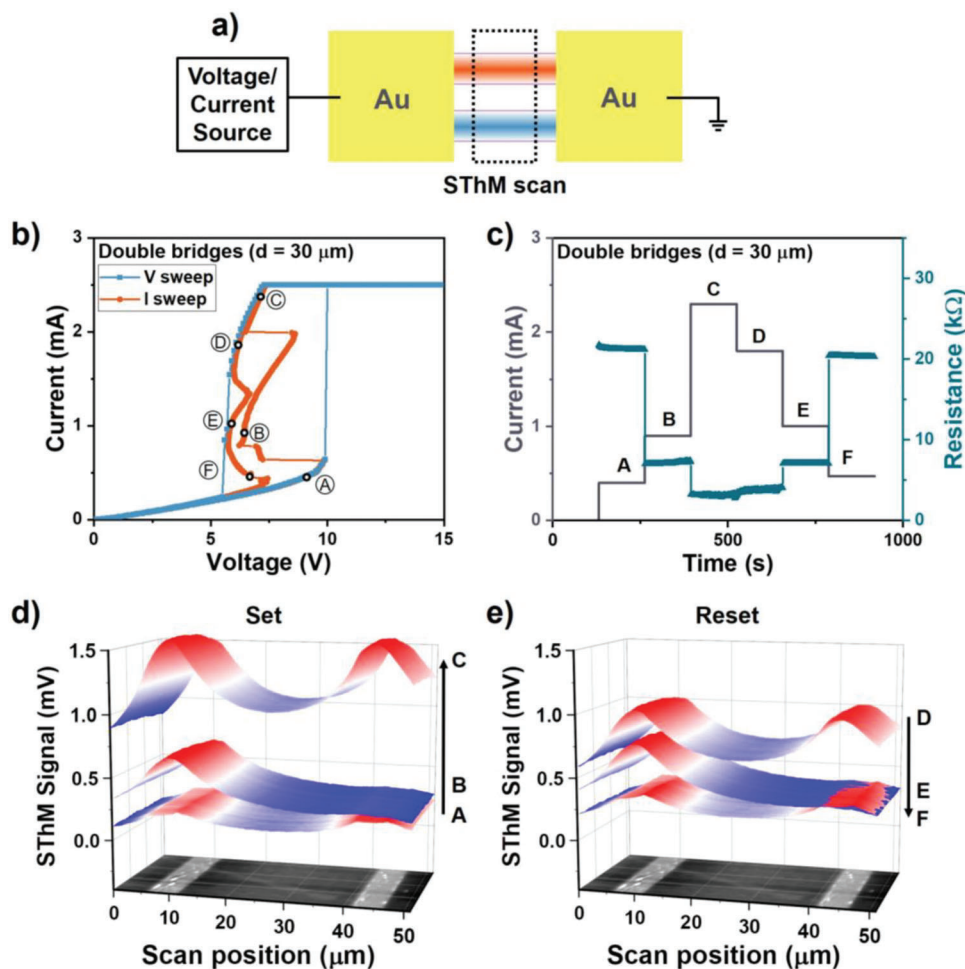
Figure 2. a) Schematic of the SThM measurement. The black dashed line box indicates the scan area. The color codes assigned to the bridges denote their status, with red indicating that the bridge is ON (i.e., low resistance), while blue represents a bridge that is OFF (i.e., high resistance). b) Voltage-controlled and current-controlled I–V characteristics of a VO_2-based double-bridge device ($L = 20$ μm, $W = 5$ μm, $d = 30$ μm). $I_{CC} = 2.5$ mA. The points where SThM measurements were taken are labeled as follows; A: 0.4 mA, B: 0.9 mA, C: 2.3 mA, D: 1.8 mA, E: 1 mA, and F: 0.47 mA. c) Applied current and measured resistance (V/I) during SThM measurements. d,e) Qualitative 3D SThM thermal maps during the set and reset process, respectively. The points where the scans were taken are indicated beside their respective maps and the arrow shows the order of the scans. The 2D surface topography images at the bottom are obtained using the SThM tip in atomic force microscopy mode and are shown as a guide for the position of the bridges in the device.

ON and OFF. Even though the bridges have been designed to be identical, slight variations in geometry, dimensions, material composition, and local defects can lead to variations in their required switching power. For the bridge that can be switched with lower power, the power for it to be switched OFF is also lower. Therefore, the first-set bridge maintains the ON state for a longer duration during the reset process.

In Figure S4 (Supporting Information), the SThM characteristics of the well-separated bridges are compared with the case for bridges in close proximity. In accordance with our observation of a single simultaneous switching of both bridges in the latter case, we see only one wide heating path covering both bridges in the SThM measurements for those devices.

Figure 3a,b shows the correlation between the switching parameters and the bridge spacing d for double-bridge devices with different bridge length, $L = 10$ and 20 μm, respectively. See Figure S6 (Supporting Information) for the voltage-sweep and

current-sweep I–V characteristics of the devices used for extracting the data. The threshold voltage V_{th} and power P_{th} in these current-controlled experiments both scale with bridge length, while the threshold current I_{th} does not. The shorter bridges can be switched individually at a smaller spacing compared with the longer bridges, which is beneficial for down scaling the device further. The power needed for the first snapback (P_1) is found to be not strongly dependent on the spacing while the power required for the second one (P_2) is correlated with the spacing. At the critical point, $d = 10$ μm in Figure 3a and $d = 20$ μm in Figure 3b and Figure S5c (Supporting Information), the first switching power is already enough for both bridges to be switched. However, due to fluctuation in the thermal cross-talk, there is also potential individual switching within the device and sometimes it dominates the switching behavior. The power difference (ΔP) between P_2 and P_1 scales with the bridge spacing, in line with the consideration that more power is required for

**ADVANCED
SCIENCE NEWS**

www.advancedsciencenews.com

**ADVANCED
ELECTRONIC
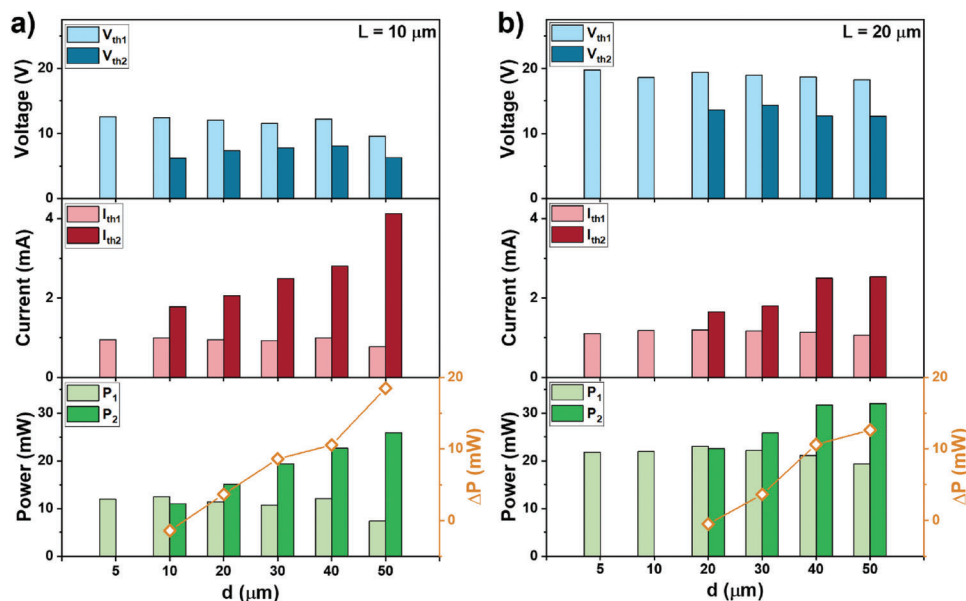MATERIALS**

www.advelectronicmat.de

Figure 3. Switching parameters of current-controlled measurements as a function of the bridge spacing for VO_2-based double-bridge devices: a) $L = 10$ μm, $W = 5$ μm and b) $L = 20$ μm, $W = 5$ μm. The top panels show the threshold voltage (V_{th}). The middle panels show the threshold current (I_{th}). The bottom panels show the calculated switching power (P_{th}) and the power difference (ΔP) between the first and the second snapback. Subscripts 1 and 2 stand for the first snapback and the second snapback, respectively.

the secondary switch when the thermal cross-talk becomes less significant.

Temperature-dependent measurements are also performed on double-bridge devices (see Figures S7 and S8, Supporting Information). With increasing operating temperature, V_s, V_h, and the hysteresis window between them for the voltage-controlled measurements reduce. For the current-controlled measurements of the device with large spacing ($d = 30$ μm), I_{th}, P, and ΔP also decrease with increasing temperature. Interestingly, the device with smaller spacing ($d = 5$ μm) starts to show individual switching when temperature increases. The critical temperature is 300 K where the device shows a secondary switch after the NDR region. When operating the device closer to the transition temperature, the amount of heating required for the transition diminishes, leading to a reduction in the required power to trigger the switching process, as well as the heating generated by the switched bridge. As a result, the influence of thermal cross-talk on the switching behavior becomes less significant.

2.2. VO2-Based Multiple-Bridge Devices

Based on the systematic studies on double-bridge devices, we further fabricated triple-bridge devices (**Figure 4**a). The addition of an extra bridge introduces the potential for more switches and resistive states. The current-sweep curves in Figure 4b show that there are three distinct snapbacks and a maximum of four stable resistive states for the triple-bridge devices. To image the switching dynamics, SThM thermal maps of each resistive state are measured (Figure 4c). It is observed that, in this particular measurement, the bridges are switched in sequence from right to left as the applied current increases, corresponding to the individual snapbacks in the I–V curves.

To obtain even more resistance states, two more bridges are added to the device design, thus forming a quintuple-bridge device (Figure 4d). As shown in Figure 4e, the current–voltage characteristics of these devices show five distinct snapbacks and a maximum of six stable resistive states, all in a single two-terminal device without additional external stimuli. The SThM thermal maps in Figure 4f show that the bridges are switched individually, in this case from the bridge in the middle to the ones at the edges. To be noted, for both triple-bridge and quintuple-bridge devices, subsequent switches predominantly happen to the neighboring bridge of the ON-state bridge for $L > d$. For $L <\approx d$, however, stochasticity can be induced as will be further discussed. This observation provides further proof that thermal cross-talk is the main influential factor for the sequential switching process.

More resistive states can be achieved by adding even more switching elements in the device and the switching principles are still maintained. However, the increasing number of VO_2 bridges also introduces more complexity and stochasticity. As can be seen in the I–V characteristics in Figure 4, before the first stable intermediate state is achieved, the competition among bridges leads to irregular patterns in the low current range. Moreover, as revealed by the SThM scans of the multiple-bridge devices (Figures S9 and S10, Supporting Information), the switching behavior after the first switch can also become complicated. For example, although the triple-bridge device in Figure 4c shows three distinct snapbacks, the order of switching bridges is completely different from the one in Figure 4b. As shown in Figure S9b,c (Supporting Information), the right bridge is set first (scans A and B), then for the second snapback, the other two OFF-state bridges are switched ON together while the right bridge is switched OFF, surprisingly (scan C). Finally, the right bridge is switched ON again creating the third snapback (scan at 2.2 mA). Even more complex phenomena are observed in the quintuple-bridge device in Figure 4f.
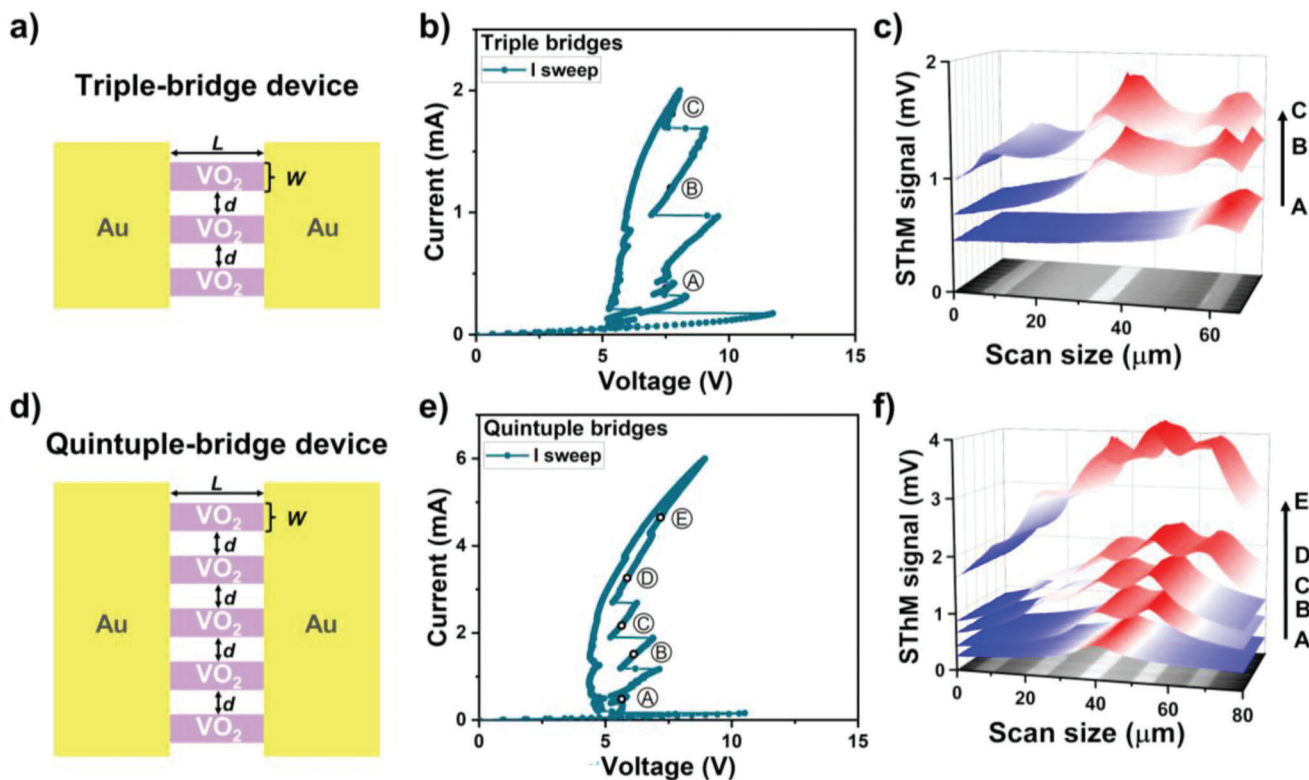
ADVANCED
SCIENCE NEWS

www.advancedsciencenews.com

ADVANCED
ELECTRONIC
MATERIALS
Open Access

www.advelectronicmat.de

Figure 4. a) Schematic of the fabricated VO$_2$-based triple-bridge device (top view). b) Current-controlled I–V characteristics and 3D SThM thermal maps during the set process of a VO$_2$-based triple-bridge devices (L = 20 µm, W = 5 µm, d = 10 µm). The points where SThM measurements were taken are labeled as; A: 0.4 mA, B: 1.2 mA, and C: 1.8 mA. d) Schematic of the fabricated VO$_2$-based quintuple-bridge device (top view). e) Current-controlled I–V characteristics and f) 3D SThM thermal maps during the set process of a VO$_2$-based quintuple-bridge devices (L = 15 µm, W = 5 µm, d = 10 µm). The points where SThM measurements were taken are labeled as follows; A: 0.4 mA, B: 1.4 mA, C: 2.2 mA, D: 3.3 mA, E: 4.9 mA).

The SThM thermal maps in Figure S10b (Supporting Information) show that the second bridge from the left appears to be set first (scan A) in a stochastic regime with probably strong competition among the bridges. At higher current, the system reaches a stable state with only the fifth-bridge switched ON (scan B). Then, the fourth bridge is triggered due to the thermal assistance of the ON-state fifth bridge (scan C). However, for the third snapback, the fourth bridge is switched OFF, whereas the second bridge is switched ON again at the same time (scan D). Subsequently, the bridges in between the second and fifth ones are triggered with the same current (scan E) as they receive nearly equal heating from their neighbors. Finally, the last remaining bridge on the left is also switched ON with increasing current. To investigate the repeatability of the behavior in the low current range, an additional round of SThM scans is performed after scan F. This time the fifth bridge is set first without competing with the second one (scan A*) and the scans at higher currents remain the same. The first switched bridge can be different for different cycles.

As discussed above, due to the additional complexity, the intrinsic switching behavior is not always as straightforward as the current-controlled I–V characteristic would indicate. The electroforming circumstances for multiple-bridge devices can be complex due to the increased number of bridges. It is expected that with sufficient power, all the bridges will undergo electroforming in the first cycle. However, in cases where the power is inadequate (Figure S1b–d, Supporting Information), only a few bridges may be formed. The competition among the nominally identical bridges for the first switch makes the set process in the low current range chaotic, leading to the unpredictable first switched bridge. Furthermore, more than one bridge can be switched ON simultaneously, sometimes accompanied by an ON-state bridge switching back to the OFF state. The surprising observation of an apparently stochastic order of switching for $L <\approx d$ cannot be explained fully by thermal cross-talk between steady-state bridges. We theorize that local thermal fluctuations could drive the observed stochasticity, which will be the subject of further research. This complexity may be further optimized and utilized in applications, for example, in finite-state machine devices.[35]

2.3. VO$_2$-Based Multiwidth-Bridge Devices

In the parallel-bridge devices, there are several variables to manipulate the switching behaviors, including the intrinsic IMT properties of the VO$_2$ bridges, the configuration of the devices, and the operating temperature. There is also an interplay between these factors, as was shown above. The intrinsic IMT determines the required switching power and the resistive states of the device. However, by tuning the operating temperature, the switching characteristic and critical spacing for synchro-
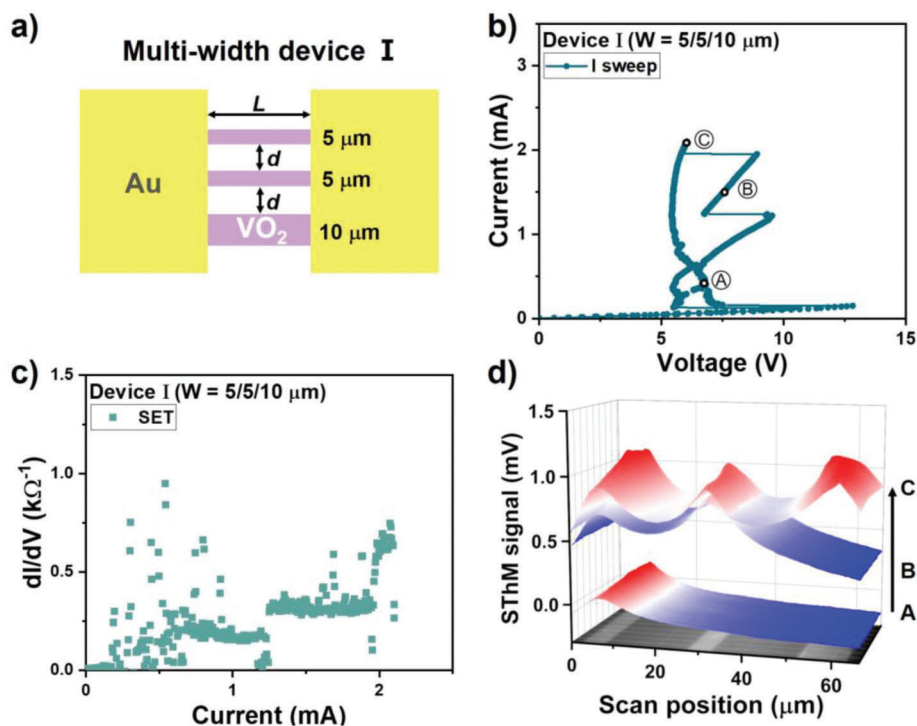
2300304 (6 of 10)

Figure 5. a) Schematic of Device I ($L = 20$ μm, $W = 5/5/10$ μm, $d = 20$ μm) (top view). b) Current-controlled $I–V$ characteristics and c) dI/dV plots of Device I. d) 3D SThM thermal maps during the set process for Device I. The points where SThM measurements were taken are labeled by letters (A: 0.4 mA, B: 1.5 mA, C: 2.2 mA).

nized/sequential/stochastic switching in multi-bridge devices can be changed. In the following, we will show an example of an additional degree of freedom, namely the geometry of the bridge.

So far, all the bridges in one device are identical with the same length, width, and spacing. However, as mentioned in a previous section, competition between identical bridges can lead to unpredictable inherent switching behavior. We expect the geometry of bridges to strongly influence the switching behavior, as it affects the initial resistance, the switching power, and the generated heating of the bridges. The measurement results of two triple-bridge devices with multiwidth bridges are shown in **Figures 5** and **6**. The devices contain bridges with the same length and spacing, but different widths and order. The wider bridge is placed at the edge of Device I (Figure 5a), and in the middle of Device II (Figure 6a). In current-controlled measurements, they both show three snapbacks and four resistive states, although the trend of the curves differs. The third switch of Device I (Figure 5b) is more intense and occurs at a lower current compared with Device II (Figure 6b). Furthermore, the dI/dV of the set process in Figure 5c indicates that there are three available current paths in Device I. The first two steps are of equal height while the third step is twice as high, suggesting the two 5 μm-wide bridges are switched first and followed by the 10 μm-wide bridge. It is confirmed by the SThM thermal maps in Figure 5d that, indeed, from the narrow one on the left to the wide one on the right the bridges are switched in sequence. In contrast, the dI/dV plots of Device II in Figure 6c are more scattered and there are only two steps with different height. The SThM measurements reveal its switching dynamics. As shown in Figure 6d, the left 5 μm-wide bridge is triggered first (scan A) and maintained ON with increas-

ing current until the device reaches a steady resistive state (scan B). However, for the second snapback, the left bridge is switched OFF and at the same time the 10 μm-wide one in the middle is triggered (scan C). Increasing the current further, the left 5 μm-wide bridge is switched ON again while the right one remains OFF (scan D).

The behavior of measured multiwidth-bridge devices shows several recurring aspects. The narrow bridges in the devices tend to win the competition in the low current range and can be triggered first. While in a zeroth-order approximation one would not expect a difference, because all W-dependencies related to power dissipation and heating cancel out, in reality additional physics play a role. Considering factors such as heat conduction through the substrate or via the electrodes, it becomes plausible that narrower bridges experience faster heating compared with wider ones. Furthermore, we can conceptualize both the narrow bridge and wide bridge as core–shell structures, following the model proposed by Li et al.[33] In this scenario, once the first metallic domains are nucleated (the "cores"), the wide bridges exhibit a lower shell resistance as compared with the narrow bridges. This implies that less current flows through the nucleated domain for the wide bridge as compared with the situation in the narrow bridge, reducing the heating process. Moreover, once the wide bridges are switched ON, they dominate most of the current flowing through the device due to their small resistance in the low-resistance state. This can also lead to narrow bridges switching back to the OFF state. If one wants to avoid this, it is wise to place the wider bridge at the edge, like in Device I.

From the examples above, it is clear that there are many possibilities for tuning the device configuration by varying the
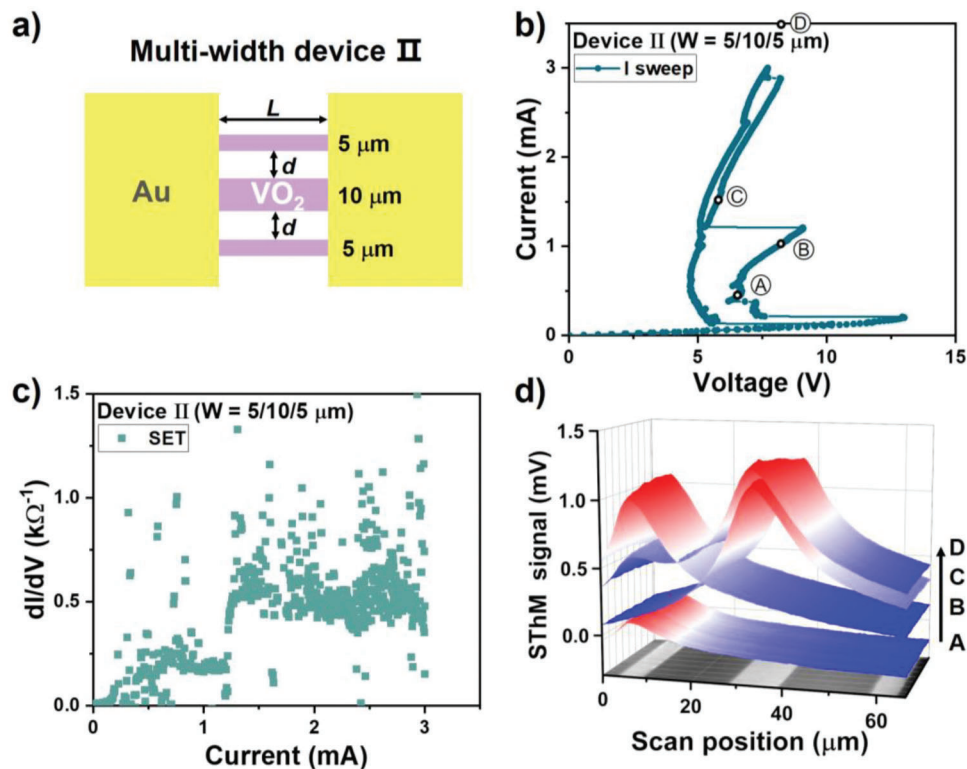
**ADVANCED
SCIENCE NEWS**

www.advancedsciencenews.com

**ADVANCED
ELECTRONIC
MATERIALS**

www.advelectronicmat.de

Figure 6. a) Schematic of Device II ($L = 20$ μm, $W = 5/10/5$ μm, $d = 20$ μm) (top view). b) Current-controlled $I–V$ characteristics and c) dI/dV plots of Device II. d) 3D SThM thermal maps during the set process for Device II. The points where SThM measurements were taken are labeled by letters (A: 0.4 mA, B: 1 mA, C: 1.5 mA, and D: 3.5 mA).

lengths, widths, and spacing of the bridges. For example, a multiple-bridge device containing bridges of different widths, growing from one side to the other, is expected to display a "waterfall switching" sequence from the narrowest bridge to the widest. The spacing can be adjusted to allow the thermal interaction assisting the subsequent switches instead of interfering with them.

3. Conclusion

In conclusion, we have investigated the resistive switching behaviors of VO$_2$-based parallel-bridge devices in a two-terminal configuration. The current-controlled measurements allow a higher degree of control over the resistive states compared with the voltage-controlled ones. The current-controlled switching behaviors are influenced by the intrinsic switching properties of the bridges and the thermal interaction among them. The switching behavior can be manipulated at the device level by adjusting several key factors, including bridge numbers, bridge spacing, and bridge geometry, which also interact with each other. With more bridges, there is potential to achieve more switching events and resistive states. The spacing between bridges affects the number of switches and the potential switching bridge. In the limit of small device length and current, stochastic behavior can emerge. Further investigations, including both modeling and experiments, are required before determining a universal criterion for distinguishing between stochastic behavior and sequential behavior. The switching principles of single-bridge devices can be extended to multiple-bridge devices, which can act as building blocks for versatile reconfigurable devices. Miniaturizing the bridges to the nanoscale will result in a significant decrease in the switching bias. A further degree of freedom that can be introduced to enhance the functionality of such VO$_2$ devices with complex topologies is the incorporation of multiple current/voltage terminals. This will be a topic of further study.

4. Experimental Section

Fabrication of VO$_2$-Based Parallel-Bridge Devices: Epitaxial VO$_2$ thin films with an estimated nominal thickness of 11 nm were deposited on single-crystal TiO$_2$ (001) substrates using pulsed laser deposition (PLD) from a polycrystalline V$_2$O$_3$ target.[8] The distance between the target and sample was ≈45 mm. A KrF excimer laser ($\lambda = 248$ nm, 20 ns pulse duration) was used with an energy density of ≈1.3 J cm^{-2} and a pulse repetition rate of 10 Hz. The growth temperature was 400 °C and the oxygen background pressure was 10^{-2} mbar. After deposition, the samples were cooled at 10 °C min^{-1} at the same oxygen pressure. X-ray diffraction (XRD) scans were performed to check the crystalline quality of the film, and atomic force microscopy (AFM) scans were conducted in tapping mode to study the surface topography. Representative XRD patterns and AFM images could be found in the previous work.[20] The as-deposited VO$_2$ films were patterned into parallel bridges with photolithography and Ar$^+$ ion beam etching.[20] Two-terminal devices were fabricated with Ti (4.5 nm)/Au (50 nm) contact pads via RF sputtering and lift-off.

Electrical Measurements: The switching characteristics of the VO$_2$-based parallel-bridge devices were investigated in a Janis cryogenic probe station with a Keithley 4200A-SCS parameter analyzer applying voltage or current sweeps at room temperature ($T_0 = 295$ K), unless otherwise stated.

**ADVANCED
SCIENCE NEWS**

www.advancedsciencenews.com

**ADVANCED
ELECTRONIC
MATERIALS**

www.advelectronicmat.de

Scanning Thermal Microscopy (SThM): SThM was performed using an Asylum AFM and an SThM thermo-resistive probe (Pd on SiN from Bruker). These SThM probes could correlate changes in their electrical resistance with temperature variations in the tip ($R_{probe} \propto T_{probe}$).[36] The SThM probe was electrically connected to an external Wheatstone bridge consisting of two fixed resistances (1 kΩ each), a potentiometer (R_{pot}), and the resistance of the probe (R_{probe}). SThM measurements were performed in passive mode, with a 0.5 V set point and a 0.5 V tip bias. The potential measured across the bridge (V_{SThM}) allowed to determine accurately the changes of the electrical resistance of the probe and, hence, temperature variations on the surface of the device. The sample was coated with a 90-nm-thick PMMA-A2 layer for the SThM scans, in order to protect the SThM tip from electrical discharges while biasing the devices. During the SThM scans, the device was biased at constant current bias values when the resistance was settled. The current was ramped up toward a maximum at which the entire device was fully switched to the low-resistance state. Afterward the current was ramped down back to 0 mA to reset the device. To probe the amount and variation of the thermal background noise, a scan with zero bias current was always performed prior to the first biased SThM scan and after the last. To be noted, the thermal signal measured from SThM could not be directly related to the surface temperature without certain calibration steps,[28] but served as a qualitative indication of the currents flowing in the bridges.

Supporting Information

Supporting Information is available from the Wiley Online Library or from the author.

Conflict of Interest

The authors declare no conflict of interest.

Data Availability Statement

The data that support the findings of this study are available from the corresponding author upon reasonable request.

[1] J. D. Kendall, S. Kumar, *Appl. Phys. Rev.* **2020**, *7*, 011305.
[2] R. Yang, H. Huang, X. Guo, *Adv. Electron. Mater.* **2019**, *5*, 1900287.
[3] G. Csaba, W. Porod, *Appl. Phys. Rev.* **2020**, *7*, 011302.
[4] P. Schofield, A. Bradicich, R. M. Gurrola, Y. Zhang, T. D. Brown, M. Pharr, P. J. Shamberger, S. Banerjee, *Adv. Mater.* **2022**, 2205294.
[5] F. J. Morin, *Phys. Rev. Lett.* **1959**, *3*, 34.
[6] J. B. Goodenough, *J. Solid State Chem.* **1971**, *3*, 490.
[7] M. M. Qazilbash, M. Brehm, B.-G. Chae, P.-C. Ho, G. O. Andreev, B.-J. Kim, S. J. Yun, A. V. Balatsky, M. B. Maple, F. Keilmann, H.-T. Kim, D. N. Basov, *Science* **2007**, *318*, 1750.
[8] J. Jeong, N. Aetukuri, T. Graf, T. D. Schladt, M. G. Samant, S. S. P. Parkin, *Science* **2013**, *339*, 1402.
[9] T. Driscoll, H.-T. Kim, B.-G. Chae, M. Di Ventra, D. N. Basov, *Appl. Phys. Lett.* **2009**, *95*, 043503.
[10] N. Vardi, E. Anouchi, T. Yamin, S. Middey, M. Kareev, J. Chakhalian, Y. Dubi, A. Sharoni, *Adv. Mater.* **2017**, *29*, 1605029.
[11] E. J. Braham, J. L. Andrews, T. E. G. Alivio, N. A. Fleer, S. Banerjee, *Phys. Status Solidi A* **2018**, *215*, 1700884.
[12] M. M. Qazilbash, M. Brehm, G. O. Andreev, A. Frenzel, P.-C. Ho, B.-G. Chae, B.-J. Kim, S. J. Yun, H.-T. Kim, A. V. Balatsky, O. G. Shpyrko, M. B. Maple, F. Keilmann, D. N. Basov, *Phys. Rev. B* **2009**, *79*, 075107.
[13] J. Jian, A. Chen, Y. Chen, X. Zhang, H. Wang, *Appl. Phys. Lett.* **2017**, *111*, 153102.
[14] D. Gu, H. Qin, X. Zhou, S. Xu, Y. Jiang, *AIP Adv.* **2018**, *8*, 015317.
[15] S. B. Lee, K. Kim, J. S. Oh, B. Kahng, J. S. Lee, *Appl. Phys. Lett.* **2013**, *102*, 063501.
[16] D. Li, A. A. Sharma, D. K. Gala, N. Shukla, H. Paik, S. Datta, D. G. Schlom, J. A. Bain, M. Skowronski, *ACS Appl. Mater. Interfaces* **2016**, *8*, 12908.
[17] J. del Valle, N. M. Vargas, R. Rocco, P. Salev, Y. Kalcheim, P. N. Lapa, C. Adda, M.-H. Lee, P. Y. Wang, L. Fratino, M. J. Rozenberg, I. K. Schuller, *Science* **2021**, *373*, 907.
[18] A. G. Shabalin, J. del Valle, N. Hua, M. J. Cherukara, M. V. Holt, I. K. Schuller, O. G. Shpyrko, *Small* **2020**, *16*, 2005439.
[19] Y. Kalcheim, A. Camjayi, J. del Valle, P. Salev, M. Rozenberg, I. K. Schuller, *Nat. Commun.* **2020**, *11*, 2985.
[20] X. Gao, C. M. M. Rosário, H. Hilgenkamp, *AIP Adv.* **2022**, *12*, 015218.
[21] A. Rana, C. Li, G. Koster, H. Hilgenkamp, *Sci. Rep.* **2020**, *10*, 3293.
[22] G. A. Gibson, *Adv. Funct. Mater.* **2018**, *28*, 1704175.
[23] A. S. Alexandrov, A. M. Bratkovsky, B. Bridle, S. E. Savel'ev, D. B. Strukov, R. S. Williams, *Appl. Phys. Lett.* **2011**, *99*, 202104.
[24] W. Yi, K. K. Tsang, S. K. Lam, X. Bai, J. A. Crowell, E. A. Flores, *Nat. Commun.* **2018**, *9*, 4661.
[25] S. M. Bohaichuk, M. Muñoz Rojo, G. Pitner, C. J. McClellan, F. Lian, J. Li, J. Jeong, M. G. Samant, S. S. P. Parkin, H.-S. P. Wong, E. Pop, *ACS Nano* **2019**, *13*, 11070.
[26] M. M. Rojo, J. Martín, S. Grauby, T. Borca-Tasciuc, S. Dilhaire, M. Martin-Gonzalez, *Nanoscale* **2014**, *6*, 7858.
[27] A. Harzheim, J. Spiece, C. Evangeli, E. McCann, V. Falko, Y. Sheng, J. H. Warner, G. A. D. Briggs, J. A. Mol, P. Gehring, O. V. Kolosov, *Nano Lett.* **2018**, *18*, 7719.
[28] T. Swoboda, N. Wainstein, S. Deshmukh, Ç. Köroğlu, X. Gao, M. Lanza, H. Hilgenkamp, E. Pop, E. Yalon, M. M. Rojo, *Nanoscale* **2023**, *15*, 7139.
[29] S. Kumar, M. D. Pickett, J. P. Strachan, G. Gibson, Y. Nishi, R. S. Williams, *Adv. Mater.* **2013**, *25*, 6128.
[30] S. Datta, *Electronic Transport in Mesoscopic Systems*, Cambridge University Press, Cambridge **1995**.
[31] B. K. Ridley, *Proc. Phys. Soc.* **1963**, *82*, 954.
[32] S. K. Nandi, S. K. Nath, A. E. El-Helou, S. Li, X. Liu, P. E. Raad, R. G. Elliman, *Adv. Funct. Mater.* **2019**, *29*, 1906731.
[33] S. Li, X. Liu, S. K. Nandi, S. K. Nath, R. G. Elliman, *Adv. Funct. Mater.* **2019**, *29*, 1905060.
[34] J. del Valle, P. Salev, F. Tesler, N. M. Vargas, Y. Kalcheim, P. Wang, J. Trastoy, M.-H. Lee, G. Kassabian, J. G. Ramírez, M. J. Rozenberg, I. K. Schuller, *Nature* **2019**, *569*, 388.
[35] L. J. Kwakernaak, M. van Hecke, *Phys. Rev. Lett.* **2023**, *130*, 268204.
[36] Y. Zhang, W. Zhu, F. Hui, M. Lanza, T. Borca-Tasciuc, M. M. Rojo, *Adv. Funct. Mater.* **2020**, *30*, 1900892.